Corrosion Science, 2004, Volume 46, Issue 2, Pages 405-425.
ISSN: 0010-938X
DOI:10.1016/S0010-938X(03)00149-5

http://www.sciencedirect.com/science/article/B6TWS-49BY0CK-1/2/14b5ff572574f531904cde6ddce82393
http://www.elsevier.com/wps/find/journaldescription.cws_home/260/description#description

Effect of applied tensile stress on intergranular corrosion of AA2024-T3

Xiaodong Liu, and G.S. Frankel
Fontana Corrosion Center, Department of Materials Science and Engineering, The Ohio State University, 477 Watts Hall, 2041 College Road, Columbus, OH 43210, USA

B. Zoofan, and S.I. Rokhlin
Department of Industrial, Welding and Systems Engineering, The Ohio State University, Columbus, OH 43210, USA

Abstract

The effect of uniaxial tensile stress on intergranular corrosion (IGC) of AA2024-T3 was studied using the foil penetration technique. Standard ASTM G49 fixed-displacement jigs were modified to allow the use of sheet samples, which were then attached to an electrochemical cell as in the foil penetration setup. The time for IGC to penetrate samples of varying thickness was monitored. This method provides a new approach to bridge the gap between IGC and intergranular stress corrosion cracking (IGSCC). Samples with various orientations relative to the rolling direction were studied in 1.0 M NaCl at controlled anodic potentials. Potentiodynamic polarization measurements indicated that the two breakdown potentials typically observed for AA2024-T3 were lower for stressed samples than for unstressed samples, and the current at a given potential was higher. The penetration rate depended on potential and was higher for stressed samples than for unstressed samples. The primary form of attack above the higher breakdown potential was IGSCC, whereas pitting dominated between the two breakdown potentials. Stress had a larger effect on penetration rate at higher applied potentials, indicating that pitting is less susceptible to the effects of stress than a properly oriented IGC crevice. The effects of stress on the penetration rates in various orientations were strongly linked to the anisotropic microstructure. X-ray microfocal radiography and optical microscopy of cross-sections were used to characterize IGSCC defects in thin penetrated foils. In certain orientations, crack faces were parallel rather than perpendicular to the stress direction as a result of the constraints of the microstructure on the orientation of the IGC. Implications for the mechanisms of IGC and IGSCC are discussed.

1. Introduction

Localized corrosion of Al alloys in aqueous chloride solutions has been investigated using different techniques [1-5]. However, few techniques exist to study the kinetics of localized corrosion growth [6,7]. Electrochemical methods typically measure current for a given potential. In order to convert current to rate, the active area needs to be known. It is often assumed that the current flows from hemispherical pits, but this is a poor assumption for localized corrosion in Al alloys.

The foil penetration technique, which was developed by Hunkeler and Bohni [8,9], is an ideal approach to determine localized corrosion growth kinetics. It is a non-electrochemical technique in which the time to penetrate a thin foil is determined by sensing the emergence of electrolyte on the backside of the foil sample. By measuring the penetration time for foils of different thickness, the depth of the fastest growing localized corrosion site as a function of time is determined. This powerful technique has been utilized by only a few investigators [10-15]. A recent study used the foil penetration technique to show that the pit growth rate in AA2024-T3 at

open circuit was strongly reduced by the presence of a small amount of dichromate in solution, whereas the growth rate at a slightly elevated applied potential was practically unchanged, even in the presence of high dichromate concentrations [11]. In another recent study, the foil penetration technique was used to show that the rate of localized corrosion growth in AA2024-T3 plate was anisotropic [12,13]. The rate of growth in the through-thickness or short transverse direction was much slower than in the longitudinal or long transverse directions. Cross-sectioning of samples proved that the growth rate was anisotropic because the attack was intergranular corrosion (IGC) and the grains were elongated in the rolling direction. The nominal growth rate in the short transverse direction was slower because of the longer path length around grains in that direction. The intergranular nature of the attack was supported by X-ray microfocal radiography analysis of penetrated foils [11].

Rota and Bohni studied IGC of an Al-4Cu-alloy aged to maximum IGC susceptibility using the foil penetration technique [14]. They then took the further step of investigating the influence of an applied tensile stress on growth kinetics of IGC [15]. Interestingly, they found the application of 80% of the proof stress had very little influence on the penetration kinetics of IGC in this alloy. The enhancement of IGC by an applied tensile stress is actually a form of stress corrosion cracking (SCC). The SCC process includes crack initiation and growth. The mechanism of crack growth involves either anodic dissolution or hydrogen embrittlement [15-19]. The grain boundary region is often the site of SCC because it can be preferentially susceptible to dissolution and is an easy ingress path for atomic hydrogen. SCC growth kinetics are usually studied with compact tension fracture mechanics specimens. The foil penetration approach can be used either with or without an applied stress, so it can be used to address the transition from IGC to IGSCC.

Rota and Bohni were not aware of the anisotropy of IGC kinetics without applied stress as was demonstrated in the recent studies, and their experiments were performed on rolled sheet with nominal growth in the through-thickness direction. The current study was undertaken to investigate the effects of stress and orientation on stress-assisted IGC growth using the foil penetration technique. X-ray microfocal radiography was also used to examine the morphology of the corrosion features.

2. Experimental

A plate of AA2024-T3 plate (Cu 4.5%, Mg 1.45%, Mn 0.57%, Si 0.11%, Fe 0.25%, Zn 0.09%, Ti 0.02%, Cr 0.01%, and other elements total 0.05% max) of thickness 1.9 cm was purchased from Metalmen Sales, Inc. Dog-bone shaped samples were machined from the plate in different orientations relative to the rolling direction. Slices of thickness 0.1-0.9 mm were then fabricated using electrical discharge machining (EDM). Details of the specimen shape are given in Fig. 1. The orientations of tested samples and the AA2024-T3 microstructure are given in Fig. 2. It should be noted that the notation of orientation shown in Fig. 2 is slightly different than the notation used in previous papers from this laboratory [12,13]. The three perpendicular directions are considered to be longitudinal (L, along the rolling direction), short transverse (S, through-thickness), and transverse (T). The orientation of a stressed sheet sample is noted by first indicating the sheet perpendicular (direction of nominal penetration) and then the stressing direction. For example, an S-L sample is stressed in the L or rolling direction, with penetration in the S or through-thickness direction. Prior to testing, the samples were polished to 1200 grit in methanol or ethanol to minimize corrosion.

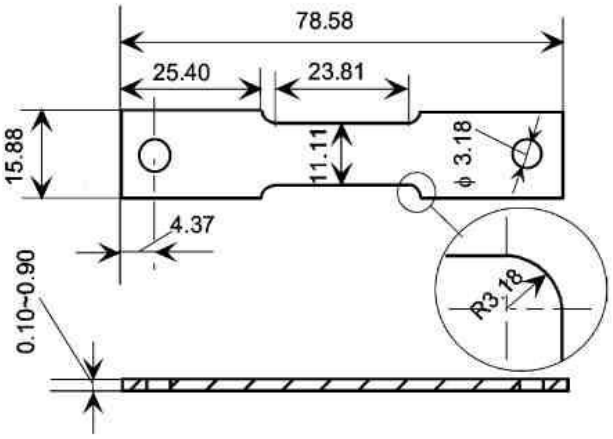

Fig. 1. Sheet sample used for stressed foil penetration experiments, all dimensions in mm.

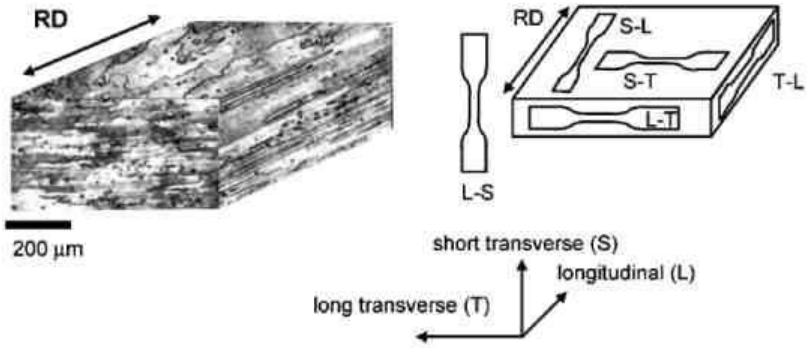

Fig. 2. Microstructure of AA2024-T3 plate and notation used for orientation of stressed sheet samples.

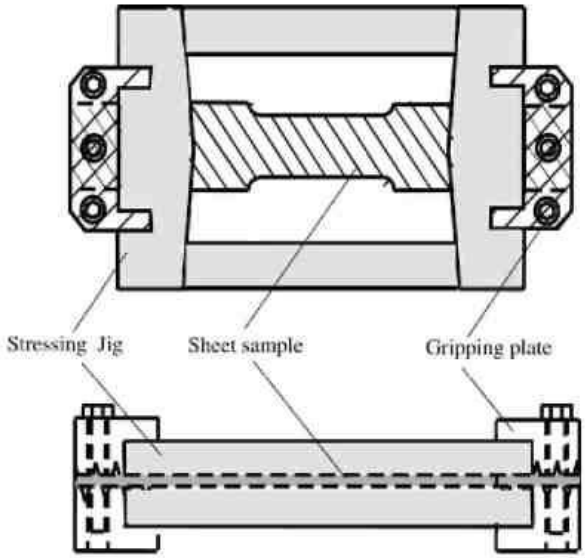

Fig. 3. Schematic of modified ASTM G49 jig used to apply constant displacement.

Rota and Bohni used a large tensile frame and ganged samples to apply a constant uniaxial load simultaneously to six samples [15]. In the current study, uniaxial stress was applied using modified ASTM G49 constant-displacement jigs (Fig. 3). Gripping plates were designed into the end pieces of the ASTM G49 test frame to handle sheet samples rather than the standard round tensile bars. A fixture is used to squeeze together the sides of the frame, which then push out the end pieces to apply a uniaxial tensile stress and a fixed displacement. A strain gauge extensometer (0.5 in. gage length, Model 3542-0100-050-ST, Interlaken Technology Corp.) was attached to the samples during the squeezing of the frame in order to sense and control the sample strain. Fig. 4 shows a stress-strain curve for an AA2024-T3 sheet in the S-T orientation measured in a standard tension testing machine. Using this stress–strain curve as a guide, strains in the elastic region were applied. Typically, a strain associated with about half of the yield stress was applied for the foil penetration testing.

The stressing jigs require the sheet samples to have a length of 79 mm, whereas the tested AA2024-T3 plate was only 19 mm in thickness. In order to study the effect of tensile stresses applied in through-thickness direction (S), extension tabs were welded to the ends of full thickness plate sections with thickness in either the L or T direction. The tabs were laser welded (at Edison Welding Institute) in an attempt to minimize the metallurgical changes associated with weld heat. Two 30 × 200 mm pieces were cut from a 2 mm thick sheet of AA2024-T3 and laser welded to either side of a 200 mm long, 2 mm thick section of the 19 mm plate that was oriented either in the L or T direction. This resulted in a 2 mm thick plate with dimensions about 79 × 200 mm containing two welds along the length. Dog-bone tensile samples were then cut from this plate, as shown schematically in Fig. 5. These samples were reduced in thickness for the penetration experiment by grinding and polishing.

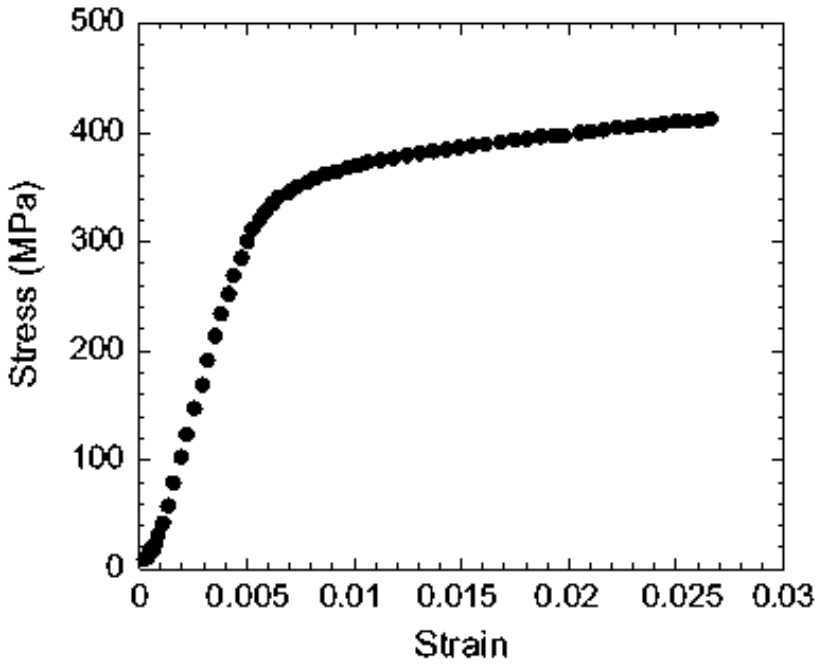

Fig. 4. Stress-strain curve for an AA2024-T3 sheet in the S-T orientation.

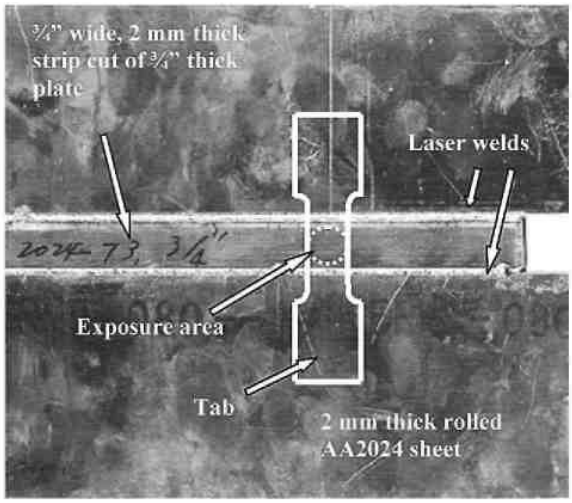

Fig. 5. Laser welded sheet sample for AA2024-T3 in the L-S orientation.

The foil penetration cell used in earlier studies had to be modified to handle the sheet sample mounted in the stressing jig. The sample was pressed against a Teflon O-ring at the bottom of a Plexiglas cell to expose an area of 1 cm^2. The sample was backed with a piece of filter paper and a Cu foil. Penetration was sensed by monitoring the resistance between the sample and the Cu foil using a detection circuit described previously [11]. A Pt counter electrode and saturated calomel reference electrode (SCE) were used in the foil penetration cell. The solution was prepared in 1 M NaCl by mixing A.C.S. grade NaCl crystals with 18.2 MΩcm Millipore deionized water.

Penetration experiments were performed under anodic potentiostatic polarization in 1.0 M NaCl solution. Oxygen was continuously bubbled into the solution during the test. Because the main goal of this study was to investigate the growth kinetics of IGC under the stress, samples were initially polarized at -0.29 V SCE for 1 s, which is similar to a traditional opening precrack in the study of SCC growth. Subsequently, the potential was stepped down to a given value and held there until the sample penetrated. The anodic current was recorded during the penetration time. Penetrated samples were cross-sectioned, polished, and examined by optical microscopy.

Anodic potentiodynamic polarization curves were measured on stressed samples in different orientations using the penetration cell and stressing jig in deaerated 1 M NaCl solution (pH = 6.1). A Gamry FAS potentiostat/galvanostat (Gamry Instruments, Inc.) system was used to control the potential. The solution was deaerated in a reservoir by Ar for 24 h before the polarization experiments. Ar gas deaerated the cell at least 15 min before filling in the solution and purged the solution continuously during the measurement. The potential was scanned at 0.1 mV/s from 30 mV below the open circuit potential (OCP) to a potential above the breakdown potentials.

Potentiostatic polarization experiments were carried out to understand the kinetics of localized corrosion at a specific potential. A sample was first potentiodynamically polarized as described above and then held at some potential for a certain time. Current was recorded during the holding time. The polarized surface was examined by optical microscopy, scanning electron microscopy (Philips XL30 FEG-SEM) and energy-dispersive X-ray spectroscopy (EDS). The

potentiostatic polarization experiments were conducted between and above the two breakdown potentials.

X-ray microfocal radiography was used as a non-destructive evaluation (NDE) method to analyze samples generated by foil penetration experiments. Sheet samples removed from the cell immediately upon penetration provide ideal samples for radiography since they are just penetrated [11,20]. NDE morphology was combined with destructive cross-sectioning to develop a full description of the corrosion sites. The morphology of the corrosion defects was found to vary strongly depending on the orientation and the application of stress.

3. Results

3.1. Potentiodynamic polarization curves of foils under stress

Representative anodic polarization curves for S surfaces with and without tensile stress are given in Fig. 6. Three replicate measurements were made for each of the conditions: unstressed S samples and stressed S-L and S-T samples. The S-L and S-T samples were loaded to an initial strain of 0.28%. The current increased quickly above the first lower breakdown potential and either reached a higher limiting value (S-L), or exhibited a peak and decreased (unstressed S and S-T). Above the second breakdown potential at higher potentials, the current increased again. The polarization curves in other orientations followed similar trends. The phenomenon of two breakdown potentials was studied in Al-4%Cu alloy in deaerated 1 M NaCl by Galvele and de Micheli [21]. They proposed that the lower breakdown potential corresponded to the dissolution of Cu-depleted zone along the grain boundary and the higher one corresponded to the dissolution of the grain bodies. Guillaumin and Mankowski gave a different explanation for the two breakdown potentials found for AA2024-T351 in aerated 1 M NaCl [22]. The lower breakdown potential was proposed to be associated with dissolution of S phase particles (Al_2CuMg) and the higher one with pits and IGC in the alloy matrix. Recently, Zhang and Frankel refined this view by describing that transient S phase attack triggers the first breakdown, and primarily IGC is responsible for the second breakdown [13].

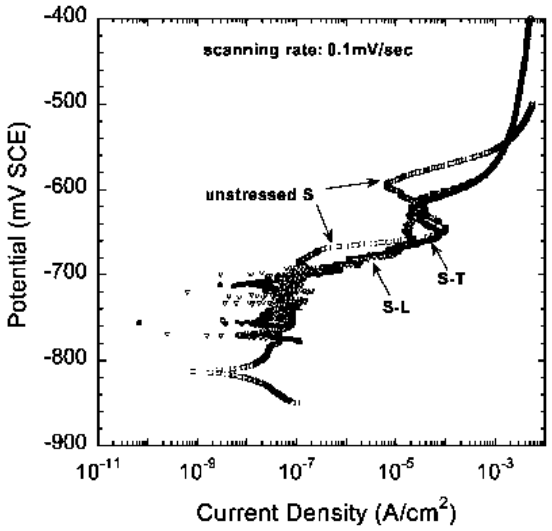

Fig. 6. Anodic polarization curves of S, S-L and S-T samples in deaerated 1 M NaCl solution.

In Fig. 6, the two breakdown potentials for stressed S-L and S-T are almost the same values, i.e. -715 to -695 and -625 to -610 mV SCE for the first and second breakdown potentials, respectively. These values are significantly lower than the counterparts for unstressed S samples: -675 to -665 and -590 to -595 mV SCE, respectively. This indicates that samples under tensile stress are more susceptible to localized corrosion in chloride solution. In the passive region, below the lower breakdown potential, the current density exhibited unstable oscillations for the stressed samples, whereas unstressed S sample maintained a steady current density. These oscillations might be associated with stress effects on induction of metastable pits, but this is still unclear. The 40 mV lower first breakdown potential for the stressed samples indicates that transient attack of S phase particles is enhanced by tensile stress. This might be an influence of stress on the S phase surface oxide film or at the particle/matrix interface. The lower second breakdown potential indicates that stress enhances IGC-initiation. Above the second breakdown potential (e.g. -580 mV SCE), the current densities of stressed S-L and S-T samples were larger than that of unstressed S by as much as a factor of 100. These findings correspond with the foil penetration results, which are described below.

3.2. Potentiostatic polarization of foils under stress

In order to understand better the effect of stress on the forms of corrosion in AA2024-T3, potentiostatic polarization was performed at different potentials. S-L samples were potentiostatically polarized at -660 mV SCE, which is between the two breakdown potentials, in deaerated 1 M NaCl for 1 or 3 h and removed from solution immediately. The morphology of the exposed surface was recorded using optical microscopy and examined by SEM and EDS. The current density recorded during potentiostatic polarization increased initially to a sharp peak and then dropped down to a low level within about 10 min (Fig. 7). The initial peak of current density was associated with initiation of localized attack, but the subsequent decrease indicates that the attack did not propagate. Fig. 8(a) is an optical microscopy image of the exposed surface. The spherical black and irregular gray particles are partially dissolved, but no intergranular attack is evident. These particles were observed by SEM as shown in Fig. 8(b) and (c). EDS analysis indicates that the spherical small S phase particles in Fig. 8(b) were depleted of Mg, and trenching occurred around the particles. The large Al-Cu-Fe-Mg particles were etched and cracked (Fig. 8(c)). These observations show that IGC does not initiate below the second breakdown potential even with applied tensile stress.

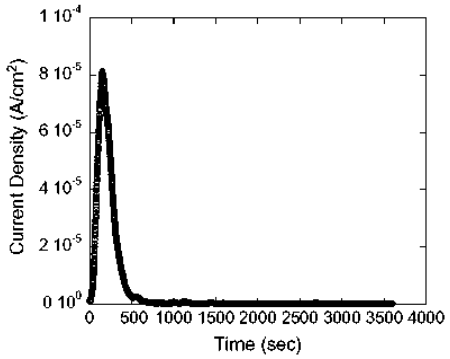

Fig. 7. Current density transient for S-L sample potentiostatically polarized at -660 mV SCE in deaerated 1 M NaCl for 1 h.

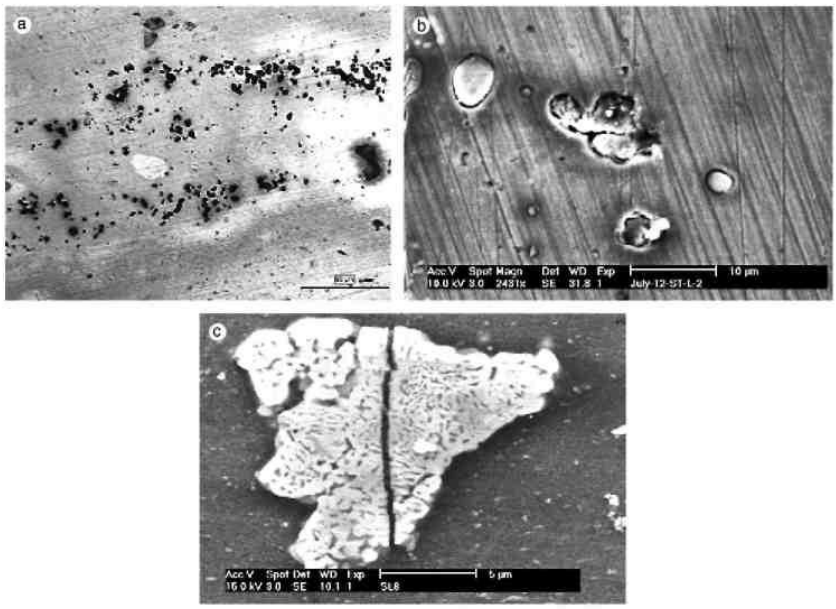

Fig. 8. Surface morphology of S-L sample exposed to deaerated 1 M NaCl at -660 mV SCE for 3 h. (a) Optical image; (b) secondary electron image of S phase particle; (c) secondary electron image of Al-Cu-Fe-Mn particle.

Potentiostatic polarization was performed above the second breakdown potential on an S–L sample in oxygenated 1 M NaCl. The sample was initially polarized at -290 mV SCE for 1 s and the potential was then stepped down to -580 mV SCE and held for 2 h. After an initial spike, the current density increased gradually (Fig. 9). Examination of the sample by optical microscopy after removal from solution indicated the presence of severe IGC dissolution and attack of some grain bodies (Fig. 10). The results are consistent with the behavior of unstressed samples [13,22], and indicate that stressed samples exhibit IGC at high potentials.

3.3. Foil penetration experiments

The foil penetration method was used to study the growth kinetics of IGC on stressed samples. Foil penetration experiments measure the penetration time for foils of varying thickness under a given condition. However, the results are typically plotted in the inverse fashion, to show depth of the fastest growing sites as a function of time. A comparison of penetration data for stressed S-T and unstressed S under applied potentials around the second breakdown potential is given in Fig. 11. At a potential above the second breakdown potential, -580 mV SCE, the growth rate of stressed S-T sample is faster than that of unstressed S. In Fig. 6, the current density of S-T during potentiodynamic polarization was shown to be much larger than that of unstressed S at -580 mV SCE. The penetration rate of S-T at -610 mV SCE is similar to that of S at -580 mV SCE. Interestingly, the current densities during potentiodynamic polarization are similar for the two conditions (Fig. 6). So despite the complications involved with determining growth kinetics directly from electrochemical measurements, the polarization curves correlate well with foil penetration data. A similar effect of potential on penetration rate has been found in L-oriented samples. Fig. 12 shows that IGC in L-T samples grows faster at -580 than at -630 mV SCE in oxygenated 1.0 M NaCl, which correlates with the higher current density at -580 than at -630 mV SCE.

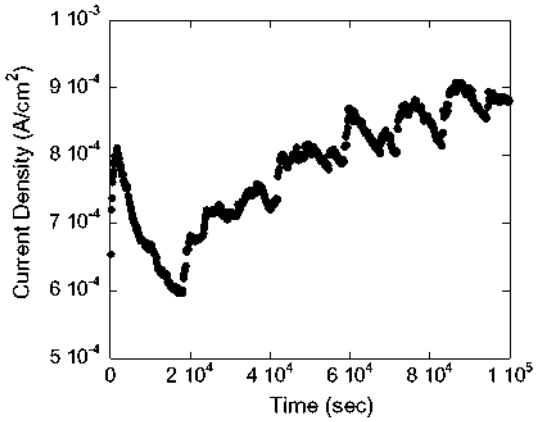

Fig. 9. Current density transient for S-L sample potentiostatically polarized at -580 mV SCE for 2 h.

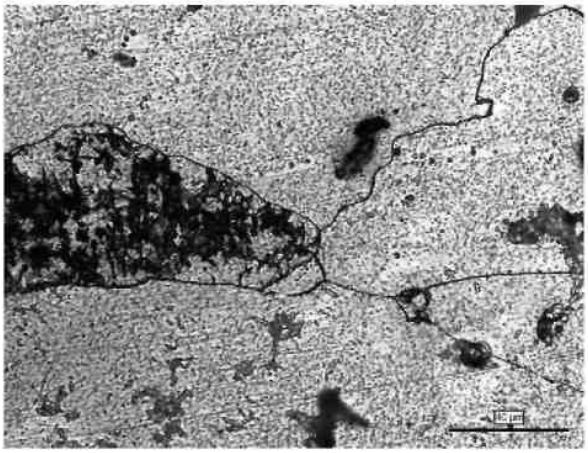

Fig. 10. Optical image of S-L sample exposed to oxygenated 1 M NaCl at -580 mV SCE for 2 h.

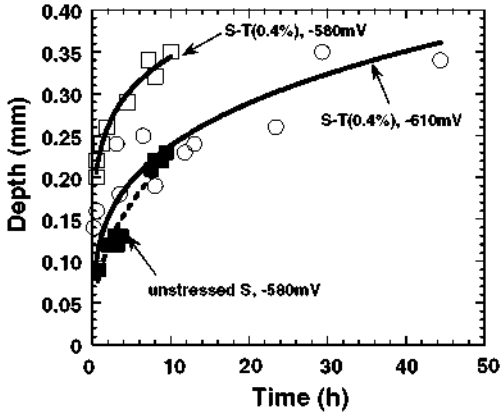

Fig. 11. Penetration data for S-oriented samples of AA2024-T3 without and with applied stress in oxygenated 1 M NaCl at -580 and -610 mV SCE. The values in parentheses are the initial strains.

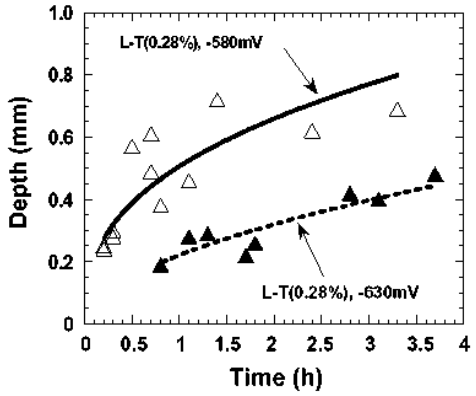

Fig. 12. Penetration data for L-oriented samples of AA2024-T3 without and with applied stress in oxygenated 1 M NaCl at -580 mV SCE and in Ar-bubbled 1 M NaCl at -630 mV SCE. The values in parentheses are the initial strains.

Fig. 13 shows foil penetration data for stressed AA2024-T3 samples in three different orientations, S-T, T-L, and L-T, at -580 mV SCE in oxygen-bubbled 1.0 M NaCl. The growth rate of the stressed samples is seen to be anisotropic, with the rate of penetration for the S-T sample being much slower than the other orientations. IGC growth anisotropy, which was previously reported for unstressed samples [12], is therefore not changed by the application of a tensile stress. The penetration depth under an applied stress for the L-T and T-L orientations was found to vary approximately with $t^{1/2}$, similar to what has been observed for pitting corrosion and IGC in unstressed samples [8,9,12].

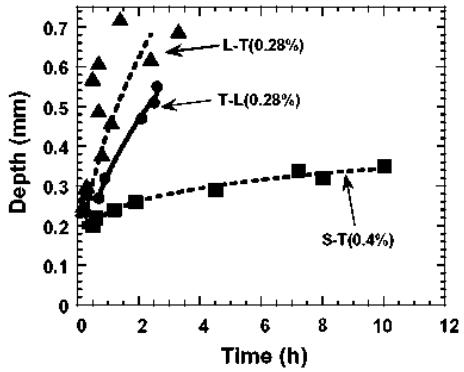

Fig. 13. Penetration data for AA2024-T3 with applied stress varying amount of fixed displacement in oxygen-bubbled 1 M NaCl at -580 mV SCE. The values in parentheses are the initial strains.

Comparisons of the penetration data for stressed and unstressed samples are given in Figs. 14-16. Fig. 14 shows data for unstressed L samples, and stressed L-T and L-S samples, Fig. 15 shows data for unstressed T samples and stressed T-L samples, and Fig. 16 shows data for the unstressed S and stressed S-L and S-T samples. In any given orientation for the L and T stressing directions, the rate of growth was slightly enhanced by the application of stress. This marginal increase resulting from the application of stress is similar to that observed by Rota and Bohni for Al-4Cu, and can be understood by considering the relationship of the stress direction to the

microstructural orientation, as shown in Fig. 2. Tensile stress applied in either the T or L direction is aligned with the elongated grain structure in the T and L sections.

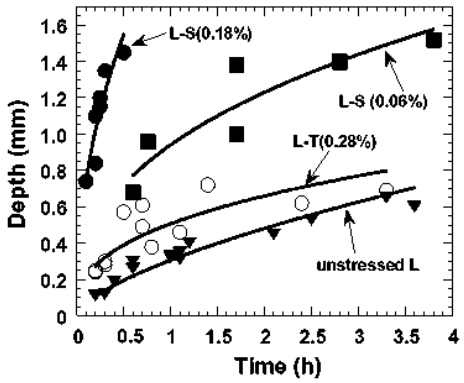

Fig. 14. Penetration data for L-oriented samples of AA2024-T3 without and with applied stress in oxygenated 1 M NaCl at -580 mV SCE. The values in parentheses are the initial strains.

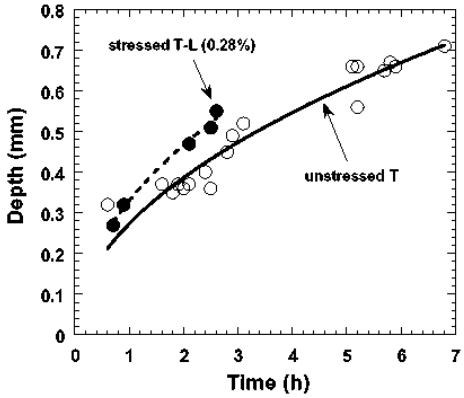

Fig. 15. Penetration data for T-oriented samples of AA2024-T3 without and with applied stress in oxygenated 1 M NaCl at -580 mV SCE. The values in parentheses are the initial strains

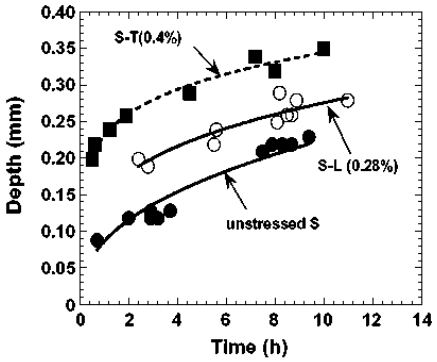

Fig. 16. Penetration data for S-oriented samples of AA2024-T3 without and with applied stress in oxygenated 1 M NaCl at -580 mV SCE. The values in parentheses are the initial strains.

On the other hand, tensile stress in the S direction is perpendicular to the elongated grain structure. Fig. 14 shows the effect of stress for penetration in the L direction (along the rolling direction). Application of a tensile strain about halfway to yield in the T direction increased the penetration rate by a small amount. In sharp contrast, application of stress in the S direction had a huge effect on the penetration rate. The application of 0.06% strain, which is barely measurable and equivalent to an applied stress of about 3 ksi, greatly increased the penetration rate. A higher strain of 0.18% increased the rate about 7× compared to the unstressed condition. This effect of stress orientation on SCC resistance has been known for some time [1,5]. However, these data show the transition from IGC to IGSCC.

The enhancement in growth kinetics with stress was greater for penetration in the S direction (S-L and S-T samples) than for either L-T or T-L samples. This may be related to the lower anisotropy of the microstructure in the S plane. The higher rate for S-T samples compared to S-L is probably associated with the fact that the T direction is the short axis of the grain structure in that plane (Fig. 2). Interestingly, when fitting the S-T and S-L data to an equation of the form $d = At^n$, the fit is better when the time exponent n is in the range of 0.15-0.26 rather than 0.5. The L-S and L-T penetration data exhibit a time exponent in the range of 0.38-0.46, which is higher, but still less than 0.5. It is possible that the growing defects resulted in a stress relaxation with time and thus a decrease in the rate of penetration with time. As described presently, the difference in growth kinetics can be explained by characterization of the corrosion defects, which were found to be IG in nature.

3.4. Characterization of the corrosion defects

X-ray radiography along with cross-sectional optical microscopy provides a full description of the corrosion defects. X-ray microfocal radiography generates a grayscale image in which the intensity depends on the integrated X-ray absorption through the sample thickness [20]. The absorption of X-rays in these samples varies with the amount of corroded material; the image on the X-ray film is a negative in that a dark region is associated with low attenuation of X-rays traveling through a region of lower density where metal was lost to corrosion. Magnification is achieved by simple optical projection from the X-ray source through the sample onto a distant film plate. The small focus spot of the electron beam that generates the X-rays results in enhanced lateral resolution in the microfocal radiography technique.

Fig. 17 shows the radiograph and optical cross-section of an unstressed S sample exposed to oxygen-bubbled 1 M NaCl at a potential of -580 mV SCE. The attack is IG in nature, as is clearly seen by the optical micrograph of the sample cross-section. The radiograph of this sample shows lots of broad and diffuse corrosion sites. The radiograph has this nature because it is a through-thickness integration of the IG attack, which spreads laterally in the foil in this orientation. The long path for IGC to propagate through S samples causes the slower penetration rate relative to the T and L orientations [12].

Fig. 18 shows an S-T sample that was penetrated at the same potential in the same solution. This image is different than that of the unstressed sample in several respects. There was much less attack in the stressed sample than in the unstressed sample. This is partly a result of the faster penetration time of the stressed sample. Furthermore, the stress concentrated the attack at cracks that were perpendicular to the applied stress direction. The higher magnification radiograph shows that the cracks were wavy and not perfectly perpendicular to the stress. As will be shown below, this is a result of the IG crack propagating around the pancake-shaped grains,

but generally maintaining a direction perpendicular to the applied stress.

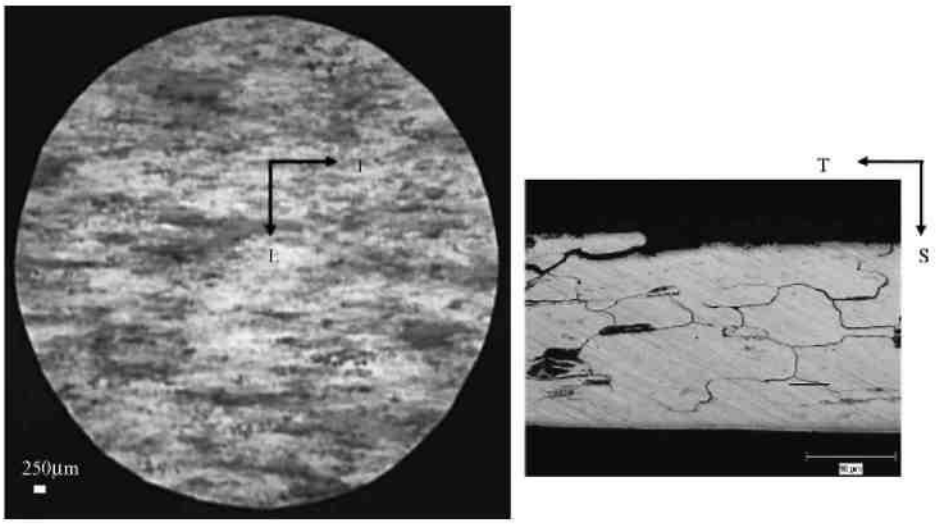

Fig. 17. AA2024-T3 S sample, 0.22 mm thick polarized at -580 mV SCE in 1 M NaCl, and penetrated in 8.2 h, unstressed. Left—radiograph, right—optical cross-section [12].

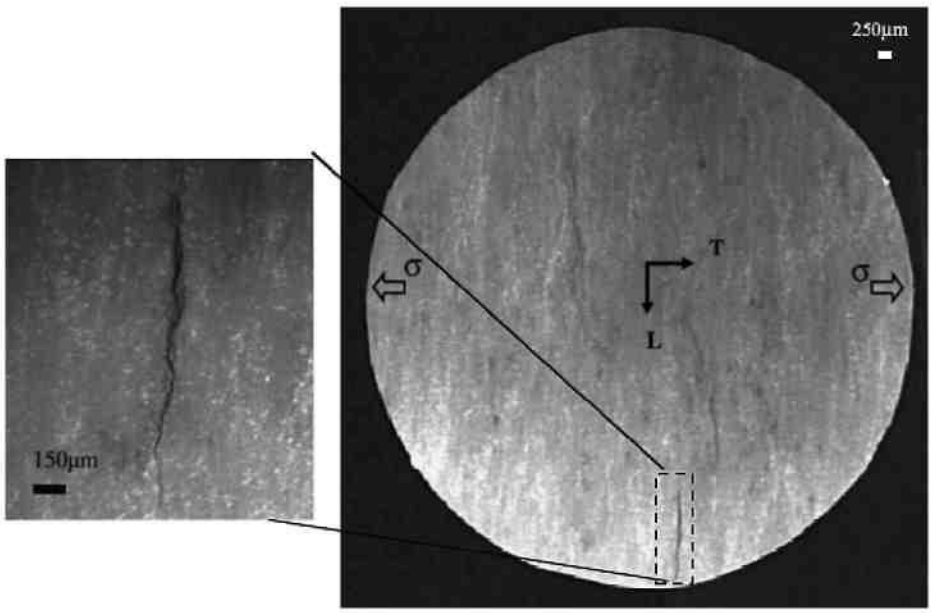

Fig. 18. AA2024-T3 S–T sample, 0.2 mm thick polarized at -580 mV SCE in 1 M NaCl, stressed. Right—radiograph, left—magnified view of crack.

An unstressed L sample exposed to the same 1 M NaCl solution at -580 mV SCE is shown in Fig. 19. The corrosion sites in the radiograph are much more focused than in the S sample shown in Fig. 17. The optical image of the cross-section shows that the IG corrosion path is essentially straight through the foil. Because of the orientation of the elongated grains, the grain boundaries go almost straight through L-oriented foils. The white spots are higher density

regions associated with inter-metallic particles. The particle number density is very high because the radiograph senses all of the particles through the whole cross-section. These particles are not evident in Fig. 17 because of all of the corrosion damage spread through the cross-section of that sample.

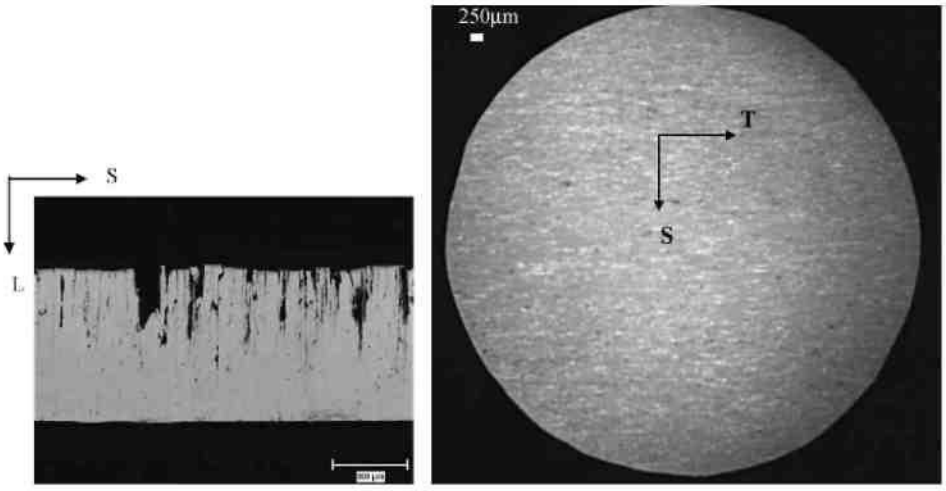

Fig. 19. AA2024-T3 L sample, polarized at -580 mV SCE in 1 M NaCl, unstressed. Left—radiograph [12], right—optical cross-section.

Images of a penetrated L-S sample are shown in Fig. 20. As for the unstressed L sample, the optical cross-section shows that the attack is straight through along the L direction. In the X-ray radiography image of this sample, the defects are seen to be elongated in the T direction and somewhat opened up in the S direction, which is the stressing direction. The optical section indicates that these defects propagate through the foil. Thus the combination of the two images provides a 3-D morphology of the defects in the L-S samples.

Unstressed T samples exhibit corrosion morphologies very similar to those shown in Fig. 19 for an unstressed L sample. The optical cross-section and radiograph for a T-L sample exposed under the same conditions but under an applied stress are given in Fig. 21. Careful examination of the defects in the radiographs shows them to be short straight cracks oriented in the direction of stress. It is quite strange to have cracks oriented in the stressing direction rather than perpendicular to the stress. However, the optical micrograph of the cross-section shows that the cracks penetrated through the thickness in the T direction, which is perpendicular to the stressing direction. (Actually, only one of them penetrated completely through.) The crack dimensions were about 50-100 µm in the L direction, but they penetrated through the 550 µm thick sample in the T direction. They were limited to the L direction in the L-S plane because of the orientation of the grains and the constraints imposed by the IGC nature of the attack.

The radiographic and optical microscopy results are combined in Fig. 22, which shows a schematic representation of the morphology of the cracks in the stressed samples. A schematic 3-D view of the elongated grain structure is also given. For the S-T sample, the cracks were perpendicular to the stress, but wavy and broad since they had to find their way between the elongated grains. The T-L sample exhibited straight cracks whose long axes were perpendicular to the stress. However, the radiography showed a projection of those cracks on the T plane. In

that projection, they appeared to be parallel to the stress. The crack faces, which were S faces, were parallel to the applied stress even though the long axis was perpendicular to the stress. It is clear that the combination of radiography and cross-sectional microscopy gives a complete picture of the cracks.

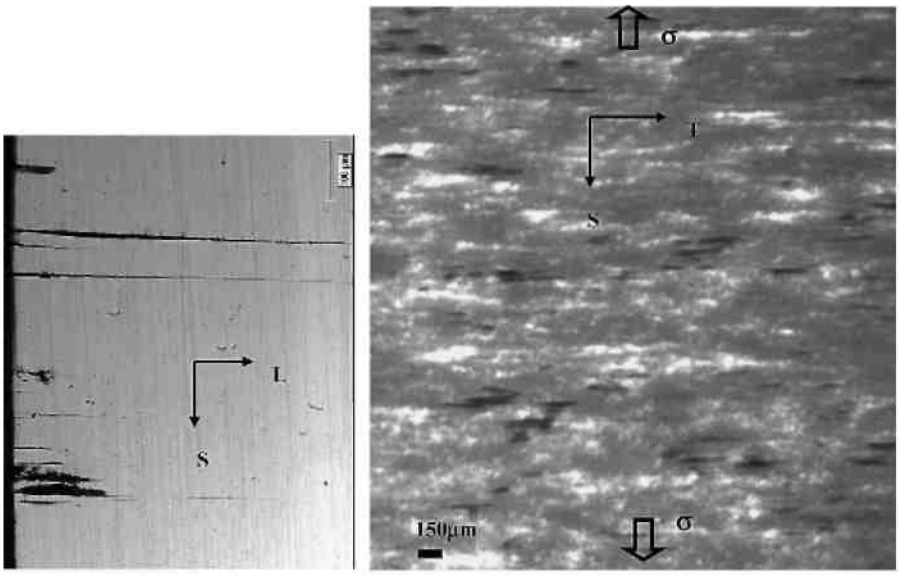

Fig. 20. Images of L-S penetrated sample at -580 mV SCE. Left—optical cross-section, right—micro-radiograph image.

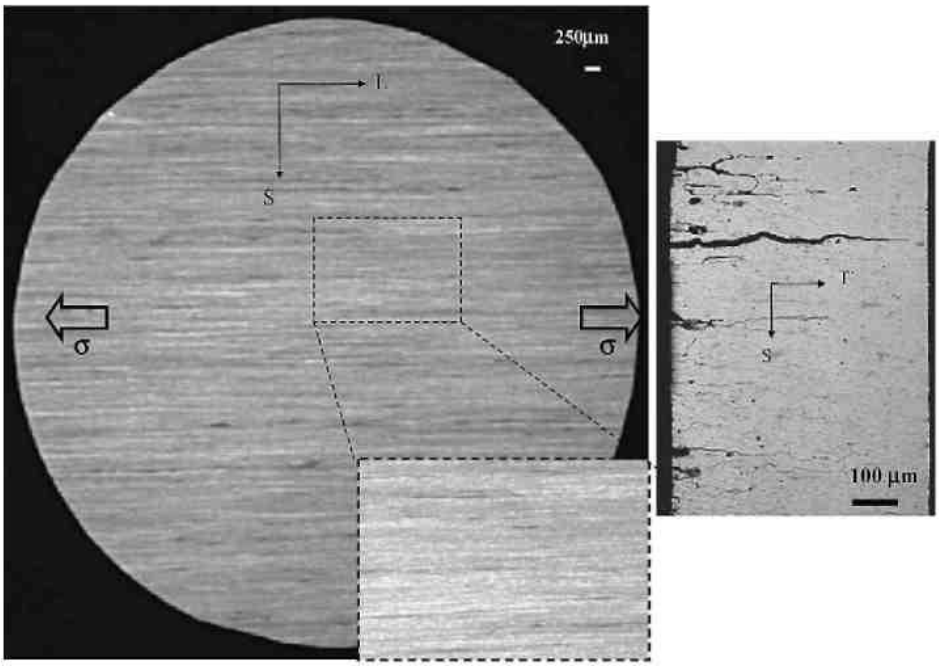

Fig. 21. AA2024-T3 T-L sample, 0.55 mm thick polarized at -580 mV SCE in 1 M NaCl, and penetrated in 2.6 h, stressed. Left—radiographs, right—optical cross-section.

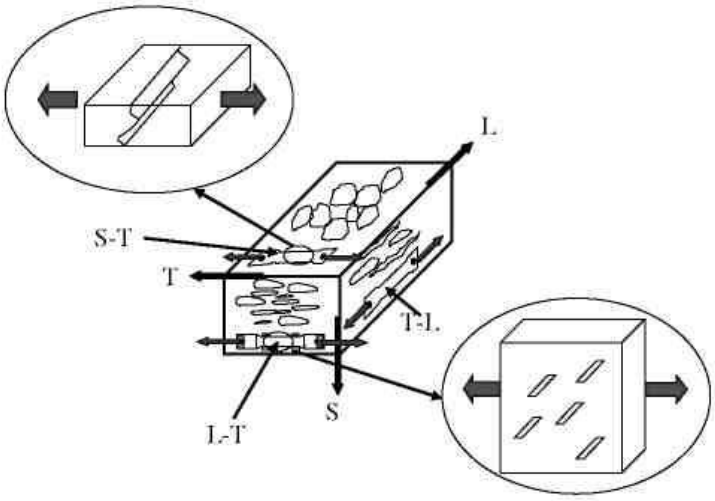

Fig. 22. Schematic representation of three-dimensional nature of the cracks in stressed foil penetration samples. Not drawn to scale.

4. Discussion

In this work, AA2024-T3 samples stressed in tension about halfway to yield exhibited a lower breakdown potential than unstressed samples. The higher current at a given potential above the breakdown potential was associated with IGC and selected grain attack. The penetration data showed that at higher potential the localized corrosion growth rate was faster for stressed samples than for unstressed samples. In particular, the growth rate of L-S samples was considerably faster than both L-T and unstressed L samples. Furthermore, the penetration rate increased with initial strain. X-ray radiography images showed that there was much less attack in S-T samples than in unstressed S samples, and that the attack was wavy and elongated rather than broad and diffuse. Because of constraints imposed by the microstructure, the cracks in the L-S samples were normal to applied stress, while those in the T-L samples were parallel to the stress direction.

Intergranular corrosion is accelerated attack at or near grain boundaries resulting from an enhanced susceptibility of the grain boundary or neighboring region. Stress corrosion cracking is driven by the synergistic actions of mechanical and electrochemical factors occurring at a crack tip. IGC and IGSCC are closely linked and even overlap in exfoliation corrosion, a form of IGC in which the stress generated by the intergranular corrosion product effectively wedges apart the elongated grain structure near the surface of wrought high strength Al alloys. One view of IGSCC is that it is simply stress-assisted IGC, though the role of hydrogen in the SCC of Al alloys has been debated. Owing to its low breakdown potential and the reactivity of freshly exposed Al surfaces (high exchange current density for hydrogen evolution), hydrogen gas is always evolved within localized corrosion sites in Al and Al alloys. Burleigh reviewed a number of studies on SCC of Al alloys and concluded that an anodic dissolution mechanism is generally favored for the 2xxx series alloys, whereas hydrogen-induced cracking is favored for 7xxx series alloys [1].

The foil penetration data shown in Fig. 14 suggest that, as stress is applied, there is a smooth transition from unstressed IGC to IGSCC, which indicates that the mechanisms for the two phenomena are similar. There can be different influences of stress on the cracking process.

Stress applied in the S direction is perpendicular to the elongated grain structure and therefore perpendicular to the IGC fissures. In this work, stress applied in the S (through-thickness) direction was extremely effective at increasing penetration rates, which is a well-known effect in SCC of Al alloys. Such stress would tend to both rupture any film that might form at the crack tip and also effectively open the crack, thereby increasing mass transport and decreasing the ohmic potential drop down the crack. Stress applied in either the L or T direction would have similar though less effective influences on intergranular fissures penetrating in the S direction. The smaller effect of stress on penetration for S-T and S-L samples relative to L-S samples is borne out by the data presented in Figs. 11 and 14.

Interestingly, the penetration rates for L-T and T-L samples are slightly larger than for the unstressed L and T samples, respectively. The microstructure constrains the IG crack faces in L-T and T-L samples to be parallel to the direction of the applied stress, and Poisson effects should generate a compressive stress in the S direction, which is perpendicular to the grain faces. Because of this, the applied stress acts to close rather than open cracks, and the accelerating effect of stress for the L-T and T-L samples is difficult to explain.

If the mechanism for IGC is the same as that for IGSCC, as indicated by the smooth transition between the two, it is possible that IGC involves a stress component even in the absence of an applied stress, like exfoliation corrosion. AA2024-T3 is susceptible to exfoliation corrosion, and it is likely that the IGC observed in the foil penetration samples would have turned into exfoliation corrosion if it were at an unconstrained surface. There is no reason to expect that the corrosion product formed during IGC would be any less voluminous than that formed during exfoliation near the surface. The constraints of the surrounding material in the foil penetration experiment prevent exfoliation for the L- and T-oriented samples. However, the voluminous corrosion still forms. It is possible that the IGC is assisted by wedging stresses generated by the corrosion product. The sample does not exfoliate because of the constraints of the sample, but the local wedging stress from the corrosion product could be significant enough to prevent repassivation in the localized corrosion environment. Nominal elastic stress on the order of half of the yield stress was shown in this work to decrease the breakdown potential in a neutral chloride environment, so it is reasonable that wedging stress in the crack environment would destabilize passivity. Once initiated, the IG cracking continues along the solute depleted zone along a grain boundary because this region is the least likely to repassivate in the localized corrosion environment. An applied stress in the S direction would clearly enhance this process. For stress applied in the L or T directions, it is likely that the compressive stress from the Poisson effect would be small compared to the wedging stress from the corrosion product. Therefore, the net effect of an applied stress in the L or T direction would be to create a biaxial stress state at the crack tip: a wedging stress from the corrosion product and a perpendicular stress along the crack width. This biaxial stress state at the crack tip would further destabilize the passive film.

Another factor that could also play a role is the fact that not all of the grain boundaries are perfectly aligned with stress applied in the L or T direction. The grains in the tested plate are certainly elongated as shown in Fig. 2. However, portions of the boundary region around most of the grains are angled away from the rolling direction to a certain extent. Any misalignment during machining of the samples would also create a situation where part of the applied stress could be resolved into a stress acting perpendicular to the boundary. As shown above, a small stress normal to the grain boundary is sufficient to accelerate growth.

5. Conclusions

The effect of uniaxial tensile stress on intergranular corrosion of AA2024-T3 was studied using the foil penetration technique in an attempt to bridge the gap between IGC and intergranular stress corrosion cracking. The following observations were made:

1. Potentiodynamic polarization measurements in 1 M NaCl indicated that the two breakdown potentials typically observed for AA2024-T3 were lower on stressed samples, and the current at a given potential was higher.
2. The penetration rate depended on potential and was higher for samples with an applied stress than for unstressed samples. Stress applied in the S direction was particularly effective at increasing penetration rates, although stress in the L and T direction also accelerated attack. The primary form of attack above the higher breakdown potential was IGSCC, whereas pitting dominated above the lower breakdown potential.
3. Stress had a larger effect on penetration rate at higher applied potentials, indicating that pitting is less susceptible to the effects of stress than a properly oriented IGC crevice.
4. The effects of stress on the penetration rates in various orientations were strongly linked to the anisotropic microstructure. X-ray microfocal radiography and optical microscopy of cross-sections were used to characterize IGSCC defects in thin penetrated foils. In certain orientations, crack faces were parallel rather than perpendicular to the stress orientation as a result of the constraints of the microstructure on the orientation of the IGC.
5. A smooth transition in penetration response with applied stress suggests that the mechanisms of IGC and IGSCC are similar. It is suggested that the stress imparted at the crack tip by the formation of a voluminous corrosion product plays an important role in IGC propagation even in the absence of an applied stress.

Acknowledgements

The authors thank Jian Xie at Edison Welding Institute for performing the laser welding. This work was supported by the United States Air Force Office of Scientific Research through Grant No. F49620-02-1-0148. The contract monitor is Lt. Col. Paul Trulove.

References

[1] T.D. Burleigh, *Corrosion* 47 (1991) 89.
[2] F.D. Wall, G.E. Stoner, *Corros. Sci*. 39 (1997) 835.
[3] A. Conde, B.J. Fernandez, J.J. De Damborenea, *Corros. Sci*. 40 (1998) 91.
[4] M.R. Bayoumi, *Eng. Fract. Mech*. 54 (1996) 879.
[5] D. Najjar, T. Magnin, T.J. Warner, *Mater. Sci. Eng*. A 238 (1997) 293.
[6] G.S. Frankel, *J. Electrochem. Soc*. 145 (1998) 2186.
[7] A. Sehgal, D. Lu, G.S. Frankel, *J. Electrochem. Soc*. 145 (1998) 2834.
[8] F. Hunkeler, H. Bohni, *Corrosion* 37 (1981) 645.
[9] F. Hunkeler, H. Bohni, *Corrosion* 40 (1984) 534.
[10] W.K. Cheung, P.E. Francis, A. Turnbull, *Mater. Sci. Forum* 192–194 (1995) 185.
[11] A. Sehgal, G.S. Frankel, B. Zoofan, S. Rokhlin, *J. Electrochem. Soc*. 147 (2000) 140.
[12] W. Zhang, G.S. Frankel, *Electrochem. Solid-State Lett*. 3 (2000) 268.
[13] W. Zhang, G.S. Frankel, *J. Electrochem. Soc*. 149 (2002) B510.
[14] A. Rota, H. Bohni, *Werkst. Korros*. 40 (1989) 219.
[15] A. Rota, H. Bohni, *Werkst. Korros*. 40 (1989) 295.

[16] R.H. Jones, R.E. Ricker, Mechanisms of stress-corrosion cracking, in: R.H. Jones (Ed.), *Stress-Corrosion Cracking, Material Performance and Evaluation*, ASM International, 1992, p. 1.
[17] H. Vogt, M.O. Speidel, *Corros. Sci*. 40 (1998) 251.
[18] V.S. Sinyavskii, *Prot. Metals* 37 (2001) 521.
[19] V.S. Sinyavskii, A.M. Semenov, *Prot. Metals* 38 (2002) 155.
[20] B. Zoofan, S.I. Rokhlin, *Mater. Eval*. 52 (1998) 191.
[21] J.R. Galvele, S.M. de Micheli, *Corros. Sci*. 10 (1970) 795.
[22] V. Guillaumin, G. Mankowski, *Corros. Sci*. 41 (1999) 421.